



LES of HCCI combustion of iso-octane/air in a flat-piston rapid compression machine

Wai Tong Chung^{a,*}, Nguyen Ly^a, Matthias Ihme^{a,b}

^a Department of Mechanical Engineering, Stanford University, Stanford, CA 94305, USA

^b SLAC National Accelerator Laboratory, Menlo Park, CA 94025, USA

Received 5 January 2022; accepted 28 July 2022

Available online xxx

Abstract

Homogeneous Charge Compression Ignition (HCCI) engines promise better efficiency and cleaner emissions than conventional piston engines, but can be challenging to control. Rapid compression machines (RCM) provide a simplified configuration for investigating HCCI combustion behavior, which is necessary for effective control of engine ignition timing and peak pressures. In this study, we assess the utility of large eddy simulations (LES) for predicting HCCI combustion in a 3-D configuration. To this end, LES with finite-rate chemistry employing a 99-species iso-octane/air mechanism of two RCM operating conditions are performed. The RCM configuration under consideration was designed by Strozzi et al. (Combust. Flame, 2019) with a flat piston to introduce large amounts of thermal stratification representative of realistic HCCI engine conditions, through the generation of corner vortices. It is shown that the simulation provides reasonable agreement with temperature fluctuations (7% difference), as well as ignition delay in the short ignition case (1 ms difference), while the long ignition case (35 ms difference) highlights more substantial deficiencies that are still within the expected uncertainty from the employed chemical mechanism. Flame propagation modes predicted by LES agree with experimental observations: spontaneous ignition is seen in the short ignition case, while deflagration is more prominent in the long ignition case. Analysis of global and local quantities classify the short ignition case in a mixed ignition regime, and the long ignition case in the mild ignition regime. These results demonstrate the utility of FRC-LES for investigations of multimode combustion regimes of HCCI combustion in a 3-D configuration.

© 2022 The Combustion Institute. Published by Elsevier Inc. All rights reserved.

Keywords: Homogeneous charge compression ignition; Multimode combustion; Rapid compression machine; Low temperature combustion; Large eddy simulation

1. Introduction

Homogeneous Charge Compression Ignition (HCCI) engines can achieve high thermal efficiency and low NO_x and soot emissions through the autoignition of homogeneous lean fuel/air mixtures [1,2]. One method for controlling peak pres-

* Corresponding author.

E-mail address: wchung@stanford.edu (W.T. Chung).

sure in HCCI engines involves introducing thermal stratification, which extends the combustion duration and lowers the peak pressure through the different ignition timing of local hot and cold gases [2]. Different levels of thermal stratification have been demonstrated to also result in different flame propagation modes through the predictive criterion developed by Sankaran et al [3]. However, precise control of HCCI can prove challenging due to a lack of detailed understanding of negative-temperature coefficient (NTC) and two-stage ignition behavior encountered in low-temperature combustion of realistic fuels, as well as the coupling between fluid dynamics and combustion chemistry.

Rapid compression machines (RCM) have been identified as canonical alternatives to optical engines for investigating HCCI combustion [4]. Previous studies [5,6] have related global turbulent and chemical timescales within experimental RCM configurations with ignition regimes linked to local flame propagation modes found in HCCI combustion.

While RCMs with creviced pistons are typically used to ensure homogeneous flow conditions, the use of flat pistons have been demonstrated to generate large-scale flow structures that can result in the thermal stratification seen in HCCI engines [7,8]. Ben-Houidi et al. [9] performed experiments in a flat-piston RCM to demonstrate its suitability for investigating HCCI combustion of heavy hydrocarbon fuels (n-hexane and an n-heptane/methylcyclohexane), to investigate ignition behavior in the NTC regime. Results validate the existence of the adiabatic core hypothesis in flat-piston RCMs, and indicate additional uncertainty in ignition delay calculations when the adiabatic core temperature falls within the NTC range. The same group then performed additional experiments with iso-octane to demonstrate the suitability of RCMs, equipped with optical access, for investigating HCCI flame propagation modes [10].

Numerical simulations provide an alternative method for investigating RCMs. Several studies [11,12] were conducted to demonstrate that ignition delay predictions from non-adiabatic 0-D homogeneous reactors agree well with multi-dimensional simulations, even with the presence of thermal stratification and multi-regime combustion modes. However, temperature inhomogeneities resulted in discrepancies in combustion duration between 0-D and multi-dimensional simulations. Stochastic reactor models can account for these discrepancies, and have been demonstrated as a low-cost simulation method for investigating the effects of mixture, temperature, and turbulent fluctuations on RCM ignition delay and combustion duration [13,14]. While these models can be applied towards relating global turbulent quantities (such as Damköhler number Da and turbulent Reynolds number Re_t) with autoignition behavior, high fidelity methods such as direct numerical simulations

(DNS) and large eddy simulations (LES) are required to rigorously investigate the interactions between flow dynamics and combustion chemistry, as well as flame propagation modes, within RCMs.

Due to large computational costs, DNS of HCCI combustion have typically been restricted to 2-D studies. Yoo et al. [15] performed 2-D DNS with a 58-species reduced n-heptane mechanism to demonstrate that thermal stratification was more important than turbulence in the resulting HCCI flame propagation mode. The same DNS dataset was then used to develop a predictive criterion for flame propagation modes based on chemical explosive mode analysis (CEMA) [16]. Luong et al. [17] investigated a 2-D DNS database consisting of nine different fuels to develop predictive criteria for HCCI ignition regimes, by extending arguments from Sankaran et al. [3].

LES provide a feasible approach for simulating 3-D flows found in experimental configurations. Yousefian et al. [18] performed inert 3-D LES of a creviced-piston RCM to demonstrate that 2-D simulations were largely valid for RCMs without large flow structures. However, in RCMs with large-flow structures, Lodier et al. [19] demonstrated that 3-D fluid dynamics was important for capturing the ignition modes, through LES and DNS, with single-step chemistry, of a flat-piston RCM [20]. Bavandla et al. [21] employed 3-D LES, with a 39-species dimethyl ether (DME) mechanism, of a flat-piston RCM to show that the accurate representation of the compression stroke was required for capturing RCM ignition behavior.

Under these contexts, the objective of this work is to evaluate the utility of 3D-LES in investigating HCCI flame propagation modes of large hydrocarbon fuels, within the NTC range, in an experimental configuration. To this end, LES, employing an arbitrary Lagrangian-Eulerian [22] control volume approach (for representing piston compression) and a 99-species iso-octane mechanism [23], of a flat piston RCM configuration [10] is performed. We present our methods in the next section, LES configuration in Section 3, results in Section 4, and conclusions in Section 5.

2. Computational methods

For the multi-dimensional simulations, we solve the Favre-filtered conservation equations for mass, momentum, energy, and chemical species:

$$\partial_t \bar{\rho} + \nabla \cdot (\bar{\rho} \tilde{\mathbf{u}}) = 0 \quad (1a)$$

$$\partial_t (\bar{\rho} \tilde{\mathbf{u}}) + \nabla \cdot (\bar{\rho} \tilde{\mathbf{u}} \tilde{\mathbf{u}}) = -\nabla \bar{p} + \nabla \cdot (\bar{\tau}_{v+t}) \quad (1b)$$

$$\partial_t (\bar{\rho} \tilde{e}_t) + \nabla \cdot [\tilde{\mathbf{u}} (\bar{\rho} \tilde{e}_t + \bar{p})] = \nabla \cdot [(\bar{\tau}_{v+t}) \cdot \tilde{\mathbf{u}}] - \nabla \cdot (\bar{\mathbf{q}}_{v+t}) \quad (1c)$$

$$\partial_t (\bar{\rho} \tilde{Y}_k) + \nabla \cdot (\bar{\rho} \tilde{\mathbf{u}} \tilde{Y}_k) = -\nabla \cdot (\bar{\mathbf{j}}_{v+t}) + \bar{\omega}_k \quad (1d)$$

with density ρ , velocity vector \mathbf{u} , pressure p , specific total energy e_t , stress tensor $\boldsymbol{\tau}$, and heat flux \mathbf{q} , Y_k , \mathbf{j}_k , and $\dot{\omega}_k$ are the mass fraction, diffusion flux, and source term for the k th species, while subscript v and t denotes viscous and turbulent quantities, respectively.

To account for mesh deformation during the compression stroke, a finite volume approach with an arbitrary Lagrangian–Eulerian scheme [22] is employed for discretizing Eq. (1):

$$\partial_t(\mathbf{V}_{cv}\mathbf{U}) = \sum_f (\mathbf{F}^v - \mathbf{F}^e - \mathbf{F}^{cv})A_f \quad (2)$$

with control volume \mathbf{V}_{cv} , face area A_f , vector of conserved variables $\mathbf{U} = [\bar{\rho}, \bar{\rho}\tilde{\mathbf{u}}, \bar{\rho}\tilde{e}_t, \bar{\rho}\tilde{Y}_k]^T$ from Eq. (1), face-normal Euler flux vector \mathbf{F}^e , and face-normal viscous flux vector \mathbf{F}^v , which corresponds to the right-hand-side of Eq. (1). \mathbf{F}^{cv} is the face-normal grid flux vector accounting for movement of the control-volume's boundaries.

Simulations are performed by employing an unstructured compressible finite-volume solver [24]. Viscous fluxes are discretized using a nominally 4th-order scheme and a sensor-based hybrid spatial discretization scheme is used for the Euler fluxes, as discussed in Ma et al. [25]. A Strang-splitting scheme is employed for time-advancement, combining a strong stability preserving 3rd-order Runge–Kutta (SSP-RK3) scheme for integrating the non-stiff operators with a semi-implicit Rosenbrock–Krylov scheme [26] for advancing the chemical source terms. A 99-species (with an additional 44 quasi-steady state species) iso-octane mechanism [23], reduced from a detailed 874-species mechanism [27], is employed for representing combustion chemistry. This mechanism was designed to represent lean HCCI combustion and have been used extensively in previous DNS studies [28]. The reduced mechanism is incorporated into the CFD solver using a Cantera library interface [29]. For the reacting LES, the Vreman model [30] is used as closure for the subgrid-scale stresses. Turbulence/chemistry interaction is accounted for using the dynamic thickened-flame model [31], employing a typical thickening factor of 5, and maximum thickening factor of 10 during late-phase combustion to resolve reaction zones near the peak pressure. Parametric studies were performed to show that this parameter does not affect the ignition delay. Outside the flame region, both turbulent Prandtl and Schmidt numbers are prescribed at constant values of 0.9.

3. Computational configuration

We perform simulations of the experimental RCM configuration of Strozzi et al. [10], featuring a combustion chamber of size $L_x \times L_y \times L_z = 50 \times 50 \times 36.5 \text{ mm}^3$ (at top-dead-center (TDC),

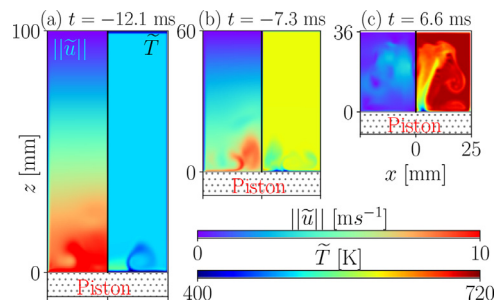


Fig. 1. Velocity (left, mirrored) and temperature (right) fields on the deforming RCM [10] quarter domain of the short ignition case at three time instances.

$t = 0 \text{ ms}$) with a square cross-section, and a flat piston. The length of the chamber at the beginning of the compression is $L_z = 456.3 \text{ mm}$, corresponding to a compression ratio of 12.5. The piston velocity during the compression phase is prescribed on the deforming control volumes (Eq. (2)) following a sine function fitted to measurements [13]. To examine different flame propagation modes in HCCI combustion, two cases are considered: (i) the short ignition case and (ii) the long ignition case. Both cases share the same initial temperature $T_0 = 294 \pm 1 \text{ K}$, compression duration $\tau_{comp} = 47.6 \text{ ms}$ and fuel/air equivalence ratio $\phi = 0.5$. The initial pressures for the short and long ignition cases are $p_0 = 1.00 \pm 0.07 \text{ bar}$ and $p_0 = 0.65 \pm 0.07 \text{ bar}$, respectively.

Fig. 1 presents the velocity and temperature fields in the deforming domain of the short ignition case for three time instances. A 0.56 M quarter domain with two symmetry boundary conditions is employed to reduce the computational expense of simulating turbulent combustion with the 99-species mechanism. A mesh convergence study and simulations of the full domain with an inert mixture were performed to demonstrate that the turbulent flow field is not affected by this reduced domain. All other boundary conditions are prescribed as isothermal walls with the initial gas temperature set to $T = T_0$. The minimum cell length at the walls was 0.08 mm corresponding to $y^+ < 10$, and the domain stretches up to a maximum cell length of 0.6 mm.

To reduce computational costs in the 3-D simulations, non-reacting simulations were first performed for the majority of the compression stroke up until $t = -3 \text{ ms}$, before beginning reacting simulations. This non-reacting duration was determined through an exhaustive parametric study performed *a priori*, which demonstrated negligible effects to the ignition delay time. 3-D simulations are performed using 1440 Intel Xeon (E5-2695) processors. The solution is advanced using a typical timestep of 120 ns, corresponding to a acoustic CFL number of 1.0, with 0.11 ms of physical time

completed in an hour wall clock time. Homogeneous reactor simulations were also performed via Cantera. Wall heat transfer in these 0-D simulations was considered with the heat loss model by Tanaka et al [32].

4. Results

Fig. 2 compares the pressure evolution of the two RCM cases from Section 3. For the short ignition case, 0-D non-adiabatic simulations performed with the LLNL 99-species (LLNL-99) reduced mechanism [23] shows slightly greater than 1 ms underprediction from experimental measurements [13], while the LLNL-874 detailed parent mechanism [27] shows less than 1 ms overprediction. The LLNL-99 mechanism demonstrates higher accuracy in ignition delay predictions than the skeletal 203-species mechanism by Jerzembeck et al. [33], which shows an overprediction of 20 ms. As such, the LLNL-99 mechanism is employed for the 3-D LES calculations.

Since 0-D non-adiabatic simulations show negligible differences in ignition delay timing from 3-D LES, 0-D LLNL-99 simulations are performed for conditions spanning upper and lower bounds of the initial conditions (Section 3) to estimate the uncertainty on the ignition delay. Results from this study demonstrate significant sensitivity to small perturbations in the initial conditions. Although the lower range of the pressure profile demonstrates that reducing the initial pressure ($p_0 = 0.93$ bar) re-

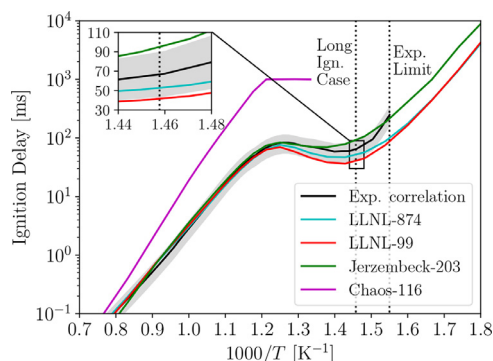


Fig. 3. Comparison of ignition delay time for four iso-octane mechanisms with an experimental correlation [34] at $p = 20$ bar. Shaded region falls within the standard deviation from the experimental scatter.

sults in better agreement with the TDC pressure measurement ($p_{TDC} = 27$ bar), an increase in the prediction of low-temperature/cool flame ignition delay τ_{ig}^{cool} by 10 ms is observed. Thus, the selection of an initial condition for the 3-D cases involves a careful balance between uncertainties from initial RCM conditions and inadequacies in the chemical mechanism in capturing first-stage/cool flame ignition [34]. In order to reduce errors in both first-stage/cool flame ignition τ_{ig}^{cool} and 2nd-stage/hot flame τ_{ig}^{hot} timing, we perform 3-D LES of the short ignition case at nominal conditions of $p_0 = 1$ bar, which results in $p_{TDC} = 29$ bar, as well as $\tau_{ig}^{cool} = 8$ ms and $\tau_{ig}^{hot} = 19$ ms, which are 5 ms greater and 1 ms less than the experiment, respectively. Following the definition from the experimental study [10], τ_{ig}^{hot} is defined as the time of peak pressure gradient $d_t p$, while τ_{ig}^{cool} is defined as the time where $d_t p > 0$ after TDC.

In the long ignition case, all simulations with reduced mechanism show negligible differences ($p_{TDC} = 20$ bar) with the experiment until TDC. After TDC, all simulations demonstrate longer τ_{ig}^{cool} , greater pressure increase during the cool flame, and shorter τ_{ig}^{hot} , when compared to the experiment. Since these discrepancies are also present, but less significant, in the 0-D simulations employing the detailed LLNL-874 mechanism, these results indicate a limitation of present capabilities for modeling combustion chemistry in the NTC range at lower pressures of heavy hydrocarbon fuels. This is consistent with the findings from a previous study [34] involving low-temperature combustion of iso-octane. Fig. 3 compares adiabatic homogeneous reactor ignition delay τ_{ig}^0 calculations, employing four mechanisms, with an experimental correlation of 661 data points from that study [34]. Large discrepancies between chemical mechanisms and the experimental corre-

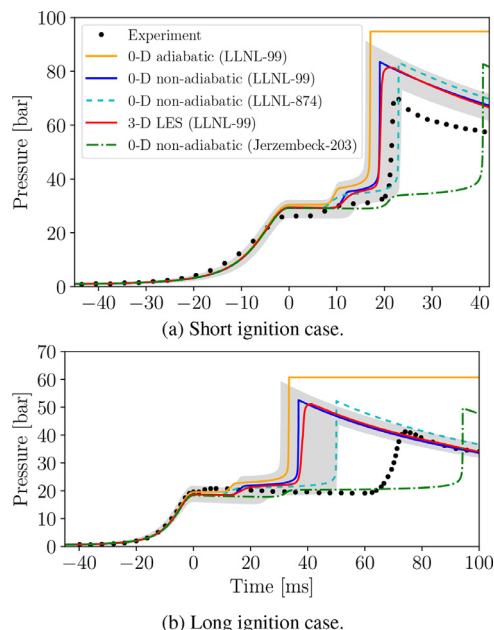


Fig. 2. Comparisons of pressure evolution from simulations of two RCM cases, with measurements [10].

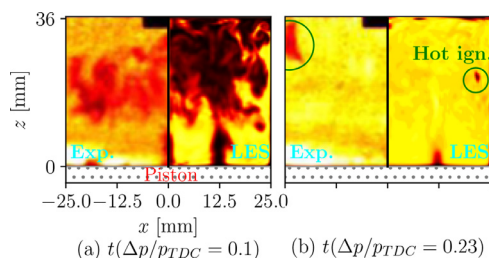


Fig. 4. Comparison of short ignition case CH_2O PLIF measurements [10] with normalized $\tilde{Y}_{\text{CH}_2\text{O}}$ field from LES during the cool flame period.

lation are observed in the NTC range, with errors in LLNL-99, LLNL-874, and Jerzembek-203 mechanisms near or within the standard deviation (34%) at TDC mean temperature ($\langle \tilde{T} \rangle = 686$ K). The 116-species mechanism by Chaos et al. [35] shows significant overprediction in ignition delay at high temperatures, and does not ignite at the investigated temperature. In Fig. 2, 3-D LES calculations show negligible differences from 0-D non-adiabatic simulations, with discrepancies in the rate of pressure increase after τ_{ig}^{hot} . The slower rise in pressure in the long ignition LES indicates deflagration as the dominant flame propagation mode, while the faster rise in pressure in the short ignition LES indicates substantial presence of spontaneous ignition modes.

Fig. 4 compares formaldehyde (CH_2O) PLIF measurements [10] with normalized $\tilde{Y}_{\text{CH}_2\text{O}}$ flowfields from the centerline plane from the short ignition LES. To compare the experiment with LES under slightly different cool flame timing and duration, we present the flowfields at times based on the normalized change of pressure $t(\Delta p/p_{TDC})$, where $\Delta p = p - p_{TDC}$. Fig. 4a show inhomogeneous CH_2O fields during the start of the cool flame, which results from thermal stratification seen within this RCM configuration. Cool flame ignition occurs first in local hot zones away from the cold gas regions (also seen in the temperature field in Fig. 1). Fig. 4b shows that the onset of hot ignition occurs in the local hot regions, where CH_2O formation first occurred, in both experiment and LES, indicating the existence of an adiabatic core in the short ignition case.

To evaluate LES predictions for turbulent and temperature fluctuations, which can impact hot flame ignition behavior [13,14], we present turbulence intensity u'/U_{comp} and normalized (with volume-averaged temperature) temperature fluctuation $\langle \tilde{T}''^2 \rangle^{1/2} / \langle \tilde{T} \rangle_{TDC}$ in Fig. 5. Here, two different turbulent modeling approaches are considered namely, the Vreman [30] subgrid-scale model and implicit LES. For both approaches, the turbulence intensity is evaluated from turbulent velocity $u' = \langle k \rangle^{1/2}$ and piston velocity scale $U_{comp} =$

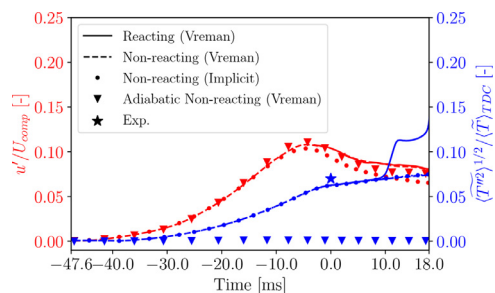


Fig. 5. Turbulence intensity u'/U_{comp} and temperature fluctuation $\langle \tilde{T}''^2 \rangle^{1/2}$ for short ignition LES prior to hot ignition.

L_z/τ_{comp} , while turbulent kinetic energy $\langle k \rangle$ is evaluated through volume-averaging along $\tilde{u}_{x,y,z}$ assuming isotropy for \tilde{u}_z , in order to separate the effect of compressive strain from $\langle k \rangle$. Turbulence is seen to increase with piston motion: LES turbulence intensity peaks ($u'/U_{comp} \approx 0.11$) at $t = -5$ ms slightly after the peak mean compression strain rate (at $t = -7$ ms) before decaying with the decelerating piston. Turbulence is seen to decay faster in the implicit LES. In contrast, the choice in turbulence modeling is shown to have negligible effects on $\langle \tilde{T}''^2 \rangle^{1/2} / \langle \tilde{T} \rangle_{TDC}$. In the non-adiabatic cases, $\langle \tilde{T}''^2 \rangle^{1/2} / \langle \tilde{T} \rangle_{TDC}$ increases rapidly with increasing piston motion, but increases at a slower rate while turbulence decays, before increasing rapidly with cool flame ignition, with LES temperature fluctuation $\langle \tilde{T}''^2 \rangle_{TDC}^{1/2} / \langle \tilde{T} \rangle_{TDC} = 0.065$ showing a 7% difference from temperature fluctuation ($\langle \tilde{T}''^2 \rangle_{TDC}^{1/2} / \langle \tilde{T} \rangle_{TDC} = 0.07$) from the corresponding experimental measurement [9]. Temperature fluctuations are not observed at any instances in the adiabatic case. Comparisons between the non-adiabatic inert and reacting Vreman cases demonstrate negligible differences for both turbulent and temperature fluctuations prior to $\tau_{ig}^{cool} = 8$ ms. This lends support for the experimental analysis [8], where temperature fluctuations from PLIF measurements of an inert RCM configuration was used to predict local flame propagation modes of a corresponding reacting methane/air mixture.

Table 1 compares the turbulent and chemical quantities extracted from reacting LES of both short and long ignition cases. Turbulence intensity ($u'_{TDC}/U_{comp} \approx 0.1$) and large-eddy length scales ($l_{TDC}/L_x \approx 0.4$) in this flat piston case are each approximately four times larger than estimated values [5] of creviced piston RCMs. These large values are consistent with experimental velocity measurements [8] and large scale flow structures observed in flat piston RCMs. This results in turbulent Reynolds numbers $Re_t = (u'l)/\nu$ (evaluated with mean viscosity ν) that are approximately an order of magnitude larger than creviced pistons.

Table 1

Turbulent and chemical quantities extracted from RCM LES, with ignition regime classification [5]. Reported experimental values [10] are shown in parenthesis, with † denoting values [8] from a different compression ratio of 18.

Case	Short ign.	Long ign.
τ_{ig}^{hot} [ms]	19.3 (20.2)	38.2 (73.5)
τ_{ig}^{cool} [ms]	7.8 (2.5)	11.4 (1.9)
u'_{TDC}/U_{comp}	0.1 (0.08†)	0.11 (0.08†)
l_{TDC}/L_x	0.40	0.36
$\tau_{u,TDC}$ [ms]	23	18
Re_t [–]	8200	5000
Da [–]	1.2	0.40
ξ [–]	0.02	–0.11
Ign. Regime	Mixed	Mild

By comparing Re_t with the Damköhler number $Da = \tau_u/\tau_{ig}^0$, evaluated as the ratio of large eddy timescale $\tau_u = l/u'$ and ignition delay of a homogeneous reactor τ_{ig}^0 , the ignition regime [5] of the two RCM cases can be identified. This can be done with the evaluation of the ratio $\xi = \log(Da)/\log(Re_t)$, which places the long ignition case in the *mild ignition* regime ($\xi < 0$), where deflagration modes are prominent, and the short ignition case in the *mixed ignition* regime ($0 \leq \xi < 0.5$), where both deflagrative and spontaneous ignition modes occur in the same domain. This classification is consistent with the different rates of pressure increment between the two cases, during hot ignition, as seen in Fig. 2.

We evaluate the normalized flowfield of planar-integrated OH mass fraction \tilde{Y}_{OH} from both LES cases, to make qualitative comparisons of hot ignition behavior with experimental broadband chemiluminescence measurements [10]. This analysis is commonly used when making qualitative comparisons between hot flame markers from LES and measurements in internal combustion engine studies [36,37]. Fig. 6a,b compares the hot flame ignition behavior between LES and the experiment in the short ignition case over the hot flame period. Near the start of the ignition (Fig. 6a) high-temperature reactions occur at regions close to the location of first ignition (see Fig. 4b). Fig. 6b shows that high-temperature reactions occur rapidly throughout the combustion chamber in both LES and the experiment in a short period of time (0.8 ms), which is indicative the existence of spontaneous ignition propagation modes. Fig. 6c,d provides a qualitative comparison of the hot flame ignition behavior between LES and the experiment, at two instances, for the long ignition case. Since a discrepancy exists in the heat release behavior when comparing LES and experiments between the end of the cool flame and the start of the hot flame, the reference time used here is based on the change of pressure at a reference pressure p_{ref} , which is the minimum pressure after the cool flame period ($p_{ref}^{exp} = 19.1$ bar and $p_{ref}^{LES} = 21.2$ bar).

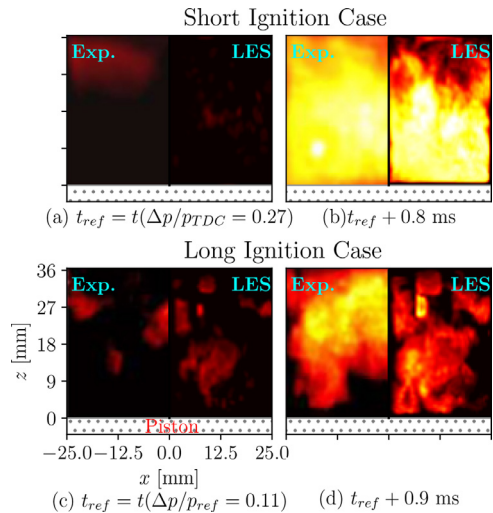


Fig. 6. Comparison of broadband chemiluminescence measurements [8] with normalized LES planar-integrated \tilde{Y}_{OH} for short and long ignition case, during the hot flame period.

Fig. 6c shows that hot ignition kernels form at random locations within the combustion chamber for both experiment and LES, before growing and merging, as shown in Fig. 6d, at a slower rate than the short ignition case. Slow flame propagation in the long ignition case indicate deflagration as the dominant mode. Despite the discrepancy in quantitative predictions in Fig. 2, LES is able to capture similar flame propagation behavior as the experiment.

To investigate flame propagation modes in both cases, we evaluate the Sankaran number [3] $Sa = \beta S_L/S_{sp}$ where $Sa > 1$ indicates deflagration, and $Sa < 1$ indicates spontaneous ignition propagation. Sa is a function of the laminar flame speed S_L , spontaneous ignition propagation speed S_{sp} , and weighting factor $\beta = 1$. $S_{sp} = (|\partial_T \tau_{ig}^0| \|\nabla \tilde{T}\|)^{-1}$ is related to the temperature gradient and homogeneous reactor ignition delay through Zeldovich's theory [38]. As performed in other works [15,23], laminar flame speeds $S_L = 0.32$ ms⁻¹ and $S_L = 0.34$ ms⁻¹ for short and long ignition cases, respectively, were evaluated through transient 1-D simulations. Fig. 7 compares temperature, temperature gradient, and ignition delay gradient fields between long and short ignition cases, at 1% heat release rate ($t = 18.1$ ms and $t = 35.1$ ms for short and long ignition cases, respectively). Spontaneous ignition modes, predicted by $Sa < 1$, are shown in black hatches, and occur more prominently in the short ignition case in gases where $|\partial_T \tau_{ig}^0|$ and $\|\nabla \tilde{T}\|$ are low. Given that temperature gradient flow fields for both short and long ignition cases are comparable in magnitude, the difference in dominant flame propagation modes between the two cases arises

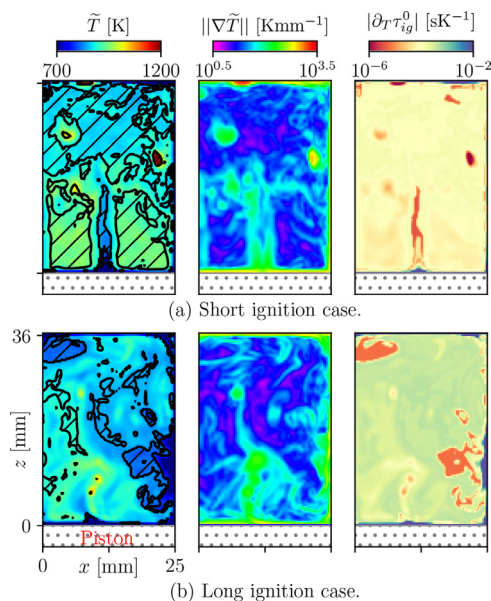


Fig. 7. Centerplane temperature, temperature gradient, and ignition delay gradient fields at 1% heat release rate. Regions with spontaneous ignition mode, predicted by Sankaran number ($Sa < 1$), are shown in black hatches.

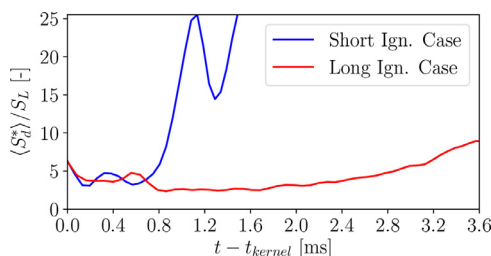


Fig. 8. Temporal evolution of 3-D LES mean displacement speed $\langle S_d^* \rangle$ after kernel formation time t_{kernel} .

from the difference in $|\partial_T \tau_{ig}^0|$, which in turn arises from different the pressure conditions.

To further examine the flame propagation modes of both cases, we compute the density-weighted displacement speed $S_d^* = [\tilde{\omega}_c - \nabla \cdot (\bar{\rho} \tilde{Y}_c \tilde{u}_c)] / (\bar{\rho}_u \|\nabla \tilde{Y}_c\|)$, which has been used to identify flame propagation modes in 2-D DNS [15,23]. The density of the unburnt $\bar{\rho}_u$ gas is evaluated with the enthalpy and pressure of the corresponding burnt gas. S_d^* is evaluated at the isoline $\tilde{Y}_c = \tilde{Y}_{CO_2} + \tilde{Y}_{CO} = 0.08$, which corresponds to the maximum heat release rate. Fig. 8 shows that both short and long ignition cases demonstrate non-monotonic behavior similar to 2-D DNS [15,17,23], which is a result of thermal runaway by heat release in the early-phase ignition kernels and compression heating during late-phase combustion. Outside of initial thermal runaway

and compressive heating, the long ignition case exhibits deflagrative combustion, indicative of the mild ignition regime. The short ignition case exhibits deflagration before $t - t_{kernel} = 0.8$ ms, after which spontaneous ignition becomes dominant, indicative of the mixed ignition regime. Kernel formation time t_{kernel} for short and long ignition cases are $t_{kernel} = 17.9$ ms and $t_{kernel} = 34.5$ ms, respectively. These results are consistent with the non-dimensional analysis presented in Table 1 and the predictive Sankaran criterion shown in Fig. 7.

5. Conclusions

LES, incorporating an arbitrary Lagrangian-Eulerian control volume approach [22] and finite-rate chemistry, of a lean premixed iso-octane/air mixture in an RCM configuration [10] is performed. Initial conditions for the two cases were selected to match two experimental conditions with different modes of flame propagation in HCCI combustion.

For the short ignition case, reasonable agreement is observed for the temperature fluctuations (7% difference), as well as cool-flame (5 ms difference) and hot-flame (1 ms difference) ignition behavior. Observed differences between LES and the experiment is explained by uncertainties from the initial conditions, and deficiencies from the low-temperature chemistry in the NTC range. In contrast, more substantial deviations (35 ms) in ignition timing are observed for the long ignition case, which can be attributed to inadequacies of the chemical mechanism in the NTC regime. However, comparisons with an experimental correlation demonstrate that the difference in ignition delay fall within the expected uncertainty within the NTC regime. Nevertheless, these results point to the need for chemical mechanisms that can accurately capture low-temperature chemistry of iso-octane.

Comparisons between experimental chemiluminescence imaging and integrated-OH LES fields shows that the simulation captures modes of flame propagation observed experimentally: the substantial presence of spontaneous ignition for the short ignition case and of deflagration for the long ignition case. These flame propagation modes were further examined by evaluating the Sankaran number. Local flame propagation modes have been related to RCM ignition regimes through global analysis of turbulent and chemical non-dimensional numbers, as well as local analysis of displacement speed, in both short ignition (mixed ignition regime) and long ignition (mild ignition regime) cases.

These results demonstrate the utility of 3-D LES for capturing and investigating multi-mode ignition and combustion processes of heavy hydrocarbon fuels in HCCI engines arising from thermal stratification. The substantial sensitivity to initial conditions, shown via homogeneous reactor calcu-

lations, indicate that 3-D LES should be combined with ensemble simulations to capture the resulting variability. These ensemble calculations should be feasible in the near future with the growth of computational power.

Declaration of Competing Interest

The authors declare that they have no known competing financial interests or personal relationships that could have appeared to influence the work reported in this paper.

Acknowledgments

The authors gratefully acknowledge financial support from the DoE under award no. DE-EE0008875, and the [National Nuclear Security Administration](#) under award no. DE-NA0003968. Resources supporting this work are also provided by the National Energy Research Scientific Computing Center, a DoE User Facility operated under contract no. DE-AC02-05CH11231. We also thank Camille Strozzi for providing the experimental data [10].

References

- [1] F. Zhao, T.N. Asmus, D.N. Assanis, J.E. Dec, J.A. Eng, P.M. Najt, Homogeneous Charge Compression Ignition (HCCI) Engines, SAE, Warrendale, PA, 2003.
- [2] M. Yao, Z. Zheng, H. Liu, Progress and recent trends in homogeneous charge compression ignition (HCCI) engines, *Prog. Energy Combust. Sci.* 35 (5) (2009) 398–437.
- [3] R. Sankaran, H.G. Im, E.R. Hawkes, J.H. Chen, The effects of non-uniform temperature distribution on the ignition of a lean homogeneous hydrogen air mixture, *Proc. Combust. Inst.* 30 (1) (2005) 875–882.
- [4] S.S. Goldsborough, S. Hochgreb, G. Vanhove, M.S. Wooldridge, H.J. Curran, C.-J. Sung, Advances in rapid compression machine studies of low- and intermediate-temperature autoignition phenomena, *Prog. Energy Combust. Sci.* 63 (2017) 1–78.
- [5] K.P. Grogan, S.S. Goldsborough, M. Ihme, Ignition regimes in rapid compression machines, *Combust. Flame* 162 (8) (2015) 3071–3080.
- [6] H.G. Im, P. Pal, M.S. Wooldridge, A.B. Mansfield, A regime diagram for autoignition of homogeneous reactant mixtures with turbulent velocity and temperature fluctuations, *Combust. Sci. Technol.* 187 (8) (2015) 1263–1275.
- [7] G. Mittal, C.-J. Sung, Aerodynamics inside a rapid compression machine, *Combust. Flame* 145 (1–2) (2006) 160–180.
- [8] C. Strozzi, A. Mura, J. Sotton, M. Bellenoue, Experimental analysis of propagation regimes during the autoignition of a fully premixed methane air mixture in the presence of temperature inhomogeneities, *Combust. Flame* 159 (11) (2012) 3323–3341.
- [9] M. Ben-Houidi, J. Sotton, M. Bellenoue, Interpretation of auto-ignition delays from RCM in the presence of temperature heterogeneities: Impact on combustion regimes and negative temperature coefficient behavior, *Fuel* 186 (2016) 476–495.
- [10] C. Strozzi, A. Claverie, V. Prevost, J. Sotton, M. Bellenoue, HCCI and SICI combustion modes analysis with simultaneous PLIF imaging of formaldehyde and high-speed chemiluminescence in a rapid compression machine, *Combust. Flame* 202 (2019) 58–77.
- [11] G. Mittal, M.P. Raju, C.-J. Sung, Computational fluid dynamics modeling of hydrogen ignition in a rapid compression machine, *Combust. Flame* 155 (3) (2008) 417–428.
- [12] N. Bourgeois, S.S. Goldsborough, G. Vanhove, M. Duponcheel, H. Jeanmart, F. Contino, CFD simulations of rapid compression machines using detailed chemistry: Impact of multi-dimensional effects on the auto-ignition of the iso-octane, *Proc. Combust. Inst.* 36 (1) (2017) 383–391.
- [13] C. Strozzi, J. Sotton, A. Mura, M. Bellenoue, Experimental and numerical study of the influence of temperature heterogeneities on self-ignition process of methane-air mixtures in a rapid compression machine, *Combust. Sci. Technol.* 180 (10–11) (2008) 1829–1857.
- [14] M. Ihme, On the role of turbulence and compositional fluctuations in rapid compression machines: Autoignition of syngas mixtures, *Combust. Flame* 159 (4) (2012) 1592–1604.
- [15] C.S. Yoo, T. Lu, J.H. Chen, C.K. Law, Direct numerical simulations of ignition of a lean n-heptane/air mixture with temperature inhomogeneities at constant volume: Parametric study, *Combust. Flame* 158 (9) (2011) 1727–1741.
- [16] T. Lu, C.S. Yoo, J.H. Chen, C.K. Law, Three-dimensional direct numerical simulation of a turbulent lifted hydrogen jet flame in heated coflow: A chemical explosive mode analysis, *J. Fluid Mech.* 652 (2010) 45–64.
- [17] M.B. Luong, F.E. Hernandez Prez, H.G. Im, Prediction of ignition modes of NTC-fuel/air mixtures with temperature and concentration fluctuations, *Combust. Flame* 213 (2020) 382–393.
- [18] S. Yousefian, N.J. Quinlan, R.F. Monaghan, Simulation of turbulent flow in a rapid compression machine: Large eddy simulation and computationally efficient alternatives for the design of ignition delay time experiments, *Fuel* 234 (2018) 30–47.
- [19] G. Lodier, C. Merlin, P. Domingo, L. Vervisch, F. Ravet, Self-ignition scenarios after rapid compression of a turbulent mixture weakly-stratified in temperature, *Combust. Flame* 159 (11) (2012) 3358–3371.
- [20] P. Guibert, A. Keromnes, G. Legros, An experimental investigation of the turbulence effect on the combustion propagation in a rapid compression machine, *Flow Turbul. Combust.* 84 (1) (2009) 79.
- [21] K.C. Bavandla, D. Zhou, A. Tripathi, Z. Sun, S. Yang, Numerical simulation of a controlled trajectory rapid compression machine, *AIAA Paper* 2020–2147 (2020).
- [22] C.W. Hirt, A.A. Amsden, J.L. Cook, An arbitrary Lagrangian–Eulerian computing method for all flow speeds, *J. Comput. Phys.* 14 (3) (1974) 227–253.

- [23] C.S. Yoo, Z. Luo, T. Lu, H. Kim, J.H. Chen, A DNS study of ignition characteristics of a lean iso-octane/air mixture under HCCI and SACI conditions, *Proc. Combust. Inst.* 34 (2) (2013) 2985–2993.
- [24] Y. Khalighi, J.W. Nichols, F. Ham, S.K. Lele, P. Moin, Unstructured large eddy simulation for prediction of noise issued from turbulent jets in various configurations, *AIAA Paper* 2011–2886 (2011).
- [25] P.C. Ma, Y. Lv, M. Ihme, An entropy-stable hybrid scheme for simulations of transcritical real-fluid flows, *J. Comput. Phys.* 340 (2017) 330–357.
- [26] H. Wu, P.C. Ma, M. Ihme, Efficient time-stepping techniques for simulating turbulent reactive flows with stiff chemistry, *Comp. Phys. Comm.* 243 (2019) 81–96.
- [27] M. Mehl, W.J. Pitz, M. Sjöberg, J.E. Dec, Detailed kinetic modeling of low-temperature heat release for PRF fuels in an HCCI engine, *SAE Paper* 2009-01-1806 (2009).
- [28] M. Ihme, W.T. Chung, A.A. Mishra, Combustion machine learning: Principles, progress and prospects, *Prog. Energy Combust. Sci.* 91 (2022) 101010.
- [29] D.G. Goodwin, R.L. Speth, H.K. Moffat, B.W. Weber, Cantera: An object-oriented software toolkit for chemical kinetics, thermodynamics, and transport processes, 2018. <https://www.cantera.org>.
- [30] A.W. Vreman, An eddy-viscosity subgrid-scale model for turbulent shear flow: Algebraic theory and applications, *Phys. Fluids* 16 (10) (2004) 3670–3681.
- [31] O. Colin, F. Ducros, D. Veynante, T. Poinot, A thickened flame model for large eddy simulations of turbulent premixed combustion, *Phys. Fluids* 12 (7) (2000) 1843–1863.
- [32] S. Tanaka, F. Ayala, J.C. Keck, A reduced chemical kinetic model for HCCI combustion of primary reference fuels in a rapid compression machine, *Combust. Flame* 133 (4) (2003) 467–481.
- [33] S. Jerzembeck, N. Peters, P. Pepiot-Desjardins, H. Pitsch, Laminar burning velocities at high pressure for primary reference fuels and gasoline: Experimental and numerical investigation, *Combust. Flame* 156 (2) (2009) 292–301.
- [34] S.S. Goldsborough, A chemical kinetically based ignition delay correlation for iso-octane covering a wide range of conditions including the NTC region, *Combust. Flame* 156 (6) (2009) 1248–1262.
- [35] M. Chaos, A. Kazakov, Z. Zhao, F.L. Dryer, A high-temperature chemical kinetic model for primary reference fuels, *Int. J. Chem. Kin.* 39 (7) (2007) 399–414.
- [36] L.M. Pickett, G. Bruneaux, R. Payri, Engine Combustion Network, 2011. <https://ecn.sandia.gov/>.
- [37] W.T. Chung, P.C. Ma, M. Ihme, Examination of diesel spray combustion in supercritical ambient fluid using large-eddy simulations, *Int. J. Engine Res.* 21 (1) (2020) 122–133.
- [38] Y.B. Zeldovich, Regime classification of an exothermic reaction with nonuniform initial conditions, *Combust. Flame* 39 (2) (1980) 211–214.